Journal of Structural Geology 32 (2010) 184–191

Contents lists available at ScienceDirect

Journal of Structural Geology

journal homepage: www.elsevier.com/locate/jsg

Compaction control of topography and fault network structure along strike-slip faults in sedimentary basins

Christoph E. Schrank*,[1], Alexander R. Cruden

Department of Geology, University of Toronto, 22 Russell Street, Toronto, ON M5S 3B1, Canada

ARTICLE INFO

Article history:
Received 14 May 2009
Received in revised form
4 November 2009
Accepted 5 November 2009
Available online 11 November 2009

Keywords:
Analogue modelling
Strike-slip faults
Topography
Compaction
Dilatancy
Shear box

ABSTRACT

Strike-slip faults commonly display structurally complex areas of positive or negative topography. Understanding the development of such areas has important implications for earthquake studies and hydrocarbon exploration. Previous workers identified the key factors controlling the occurrence of both topographic modes and the related structural styles. Kinematic and stress boundary conditions are of first-order relevance. Surface mass transport and material properties affect fault network structure. Experiments demonstrate that dilatancy can generate positive topography even under simple-shear boundary conditions. Here, we use physical models with sand to show that the degree of compaction of the deformed rocks alone can determine the type of topography and related surface fault network structure in simple-shear settings. In our experiments, volume changes of ~5% are sufficient to generate localized uplift or subsidence. We discuss scalability of model volume changes and fault network structure and show that our model fault zones satisfy geometrical similarity with natural flower structures. Our results imply that compaction may be an important factor in the development of topography and fault network structure along strike-slip faults in sedimentary basins.

1. Introduction

Strike-slip faults occur from plate-boundary to local scales and their rich structural inventory is important for the exploration and development of hydrocarbon deposits in sedimentary basins (Harding, 1985; Sylvester, 1988). Strike-slip faults appear as narrow linear features at the surface with lengths up to thousands of kilometres. In detail, they consist of a complex, anastomosing network of smaller faults. Within these networks, areas of either positive or negative topography occur on various scales, e.g., pressure ridges, sag ponds, positive and negative flower structures, pop-ups, and pull-apart basins (Bergerat et al., 2003; Harding, 1985; Mann, 2007; Sylvester, 1988).

Stress- and kinematic-boundary conditions exert the first-order control on the generation of topography and fault network structure (Braun, 1994; Dresen, 1991; Koons and Henderson, 1995; Mann, 2007; Naylor et al., 1986; Richard et al., 1995). A component of fault-normal stress seems required to create topography. However, numerical (Braun, 1994) and physical (Le Guerroué and Cobbold, 2006; Schöpfer and Steyrer, 2001) models show that dilatancy can induce positive topography in simple-shear settings. Host rock rheology (Dresen, 1991), the thickness of the sheared rock layer (Schöpfer and Steyrer, 2001; Tchalenko, 1970), and syndeformational erosion and sedimentation (Le Guerroué and Cobbold, 2006) affect fault network structure but do not switch the polarity of topography. Here we use analogue experiments with sand to show that the degree of compaction of the deformed rock can determine the topographic mode and invoke characteristic differences in surface fault network structure. This has important implications for strike-slip faults in sedimentary basins.

2. Methods

We performed ten experiments with loosely and densely packed sand. Since the results are consistent with respect to fault zone width, number of faults, and topography, only two representative experiments are shown. We use a simple-shear box with side walls and a basal cut as velocity discontinuity (Fig. 1a). One half of the box is driven by a piston at a constant rate of 2.5 cm/h. A 4 cm thick layer of quartz sand with a mean grain size of 200 μm is employed as analogue for upper-crustal brittle rocks (Lohrmann et al., 2003). We varied its physical properties by sifting or pouring it into the box (Krantz, 1991). The sifted sand has a density of 1700 kg/m^3 and rheology, determined in a Hubbert-type shear apparatus with Plexiglas walls similar to that used by Lohrmann et al. (2003),

* Corresponding author. Tel.: +61 8 6488 2680; fax: +61 8 6488 1037.
E-mail address: cschrank@cyllene.uwa.edu.au (C.E. Schrank).
[1] Present address: School of Earth and Environment, The University of Western Australia, 35 Stirling Highway, Crawley, WA 6009, Australia.

0191-8141/$ – see front matter © 2009 Elsevier Ltd. All rights reserved.
doi:10.1016/j.jsg.2009.11.003

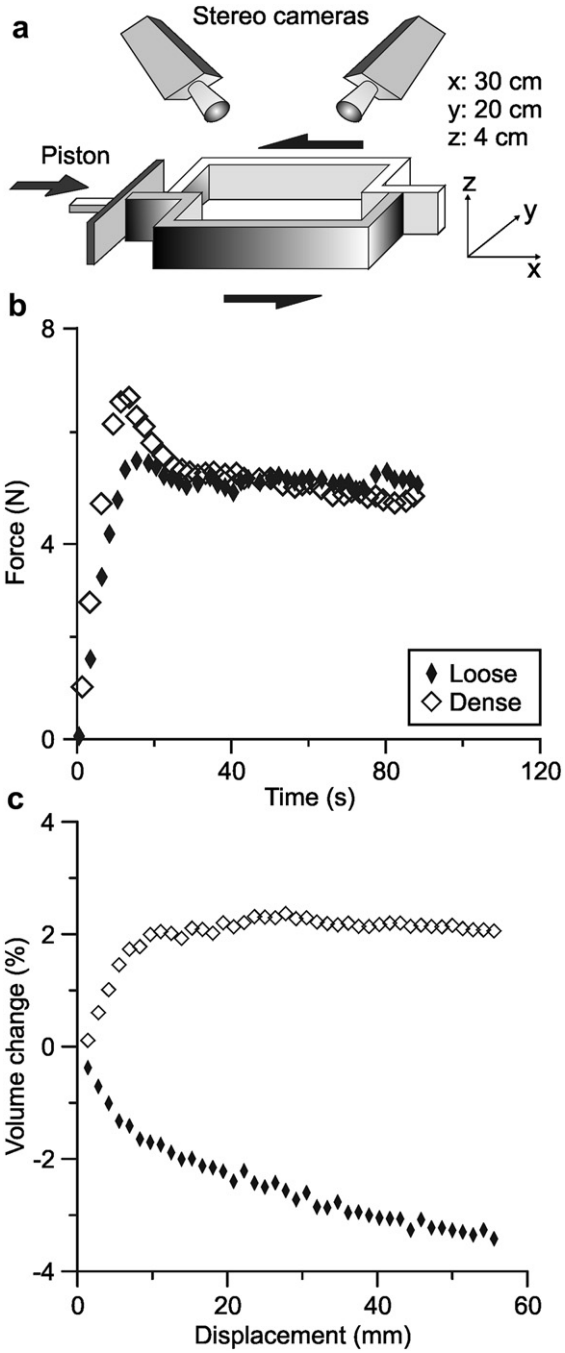

Fig. 1. a) Experimental setup. Box dimensions with respect to coordinate system are given in figure. b) Results of a Hubbert-type shear test on a 4 cm layer of loose and dense sand, respectively. c) Plots of total-volume change as a function of piston displacement in models with loose and dense sand.

characterized by transitional strain hardening, followed by strain softening until stable strength is reached (Lohrmann et al., 2003) (Fig. 1b). The peak and stable friction angles are 39° and 27°, respectively. Assuming a quartz grain density of 2660 kg/m^3, the sifted sand has a porosity of 36.1%. Pouring results in a higher filling velocity and under-compacted sand with a density of 1474 kg/m^3, porosity of 44.6%, and peak and stable friction angles 30° and 27°, respectively. Cohesion at peak strength is 60 and 80 Pa for sifted and poured sand, respectively, with an uncertainty of ~30% inherent to the measurement method (Lohrmann et al., 2003). Since the basal normal stresses in our experiments exceed 570 Pa, the critical stress is friction-controlled.

We note that the above mechanical data do not account for side-wall friction of the shear apparatus. Mourgues and Cobbold (2003) point out that a silo effect can lead to an overestimation of normal stress in shear tests and therefore erroneous friction coefficient and cohesion values. If we apply the correction given by Mourgues and Cobbold (2003) assuming a friction coefficient, μ_s, of 0.35 between the shear box walls (Plexiglass) and our sand and a ratio of horizontal to vertical stress, K, of 0.5, we obtain peak and stable friction angles of ~50° and ~36°, respectively, for sifted sand, and ~40° and ~36° for poured sand. The cohesion values decrease to 20 Pa and 37 Pa for sifted and poured sand, respectively. This correction is sensitive to the choice of μ_s and K, which are assumed here to be similar to those of the experiments of Mourgues and Cobbold (2003). However, in this paper, we focus on the effect of differences in initial porosity of sand (i.e., its degree of compaction) on strike-slip experiments. The given mechanical data (friction-corrected and -uncorrected) bracket the true properties of our sand, and a more precise mechanical characterization is beyond the scope of this work.

We monitored the experiments with a stereoscopic 3D Particle Imaging Velocimetry (PIV) system (manufactured by LaVision GmbH, Germany). Images were recorded every 100 s with two monochrome CCD cameras from above (Fig. 1a) providing 3D measurements of the model surfaces with an accuracy of 0.1 mm. The resulting digital elevation models were used to compute volume changes by subtracting the initial undeformed model surface from deformed model surfaces over time. Camera resolution was ~90 pixel/cm. 3D surface velocity fields are derived by cross-correlation of sequential images (Adam et al., 2005). We determined 3D surface displacement vectors in a ~16 × 14 cm^2 area in the box centre with an accuracy of <0.1 mm for 2 × 2 mm^2 search windows. Strains were calculated from the displacement gradients.

3. Results

The differences in topographic evolution for loose and dense sand are striking. In loose sand, the whole surface begins to subside towards the piston at the onset of deformation (Fig. 2). The asymmetry of the subsidence is attributed to vibrations transmitted from the stepper motor close to the piston. A channel-like basin propagates along the fault system towards the rear end of the model (Figs. 2 and 3). A rhomb-shaped basin, similar to a pull-apart basin, opens in the model centre (Fig. 2b,c). Maximum elevation difference is ~5 mm. The total volume decreases by 3.4% (Fig. 1c), the volume within the fault zone alone decreases by 4.2%. In contrast, positive topography develops in dense sand. It is focused in a fault-bound wedge in the model centre (Figs. 2 and 3). Topographic growth becomes increasingly localized, the maximum elevation difference is 7 mm and the maximum total volume increase is 2.4% (Fig. 1c). Volume increase in the wedge alone amounts to 5.1%.

The surface fault network geometry differs accordingly, as illustrated by maps of incremental horizontal shear strain $Exy = \mathrm{d}D_x/\mathrm{d}y$, where D_x is displacement in x-direction, and transversal shear strain profiles through the model centre (Fig. 3). The strain increments correspond to 0.7 mm displacement steps. Loose sand displays a narrow fault network consisting of synthetic Riedel shears linked by P and Y shears (Tchalenko, 1970). Dense sand develops a broader fault network comprising three main faults in synthetic Riedel orientation. The outer faults bound the wedge while the middle fault is in its centre. Initially, the middle fault consists of linked synthetic Riedel shears that are visible but below PIV resolution. At later stages the entire fault network is dominated by large Riedel shears that are less strongly linked at the surface and longer than those in loose sand.

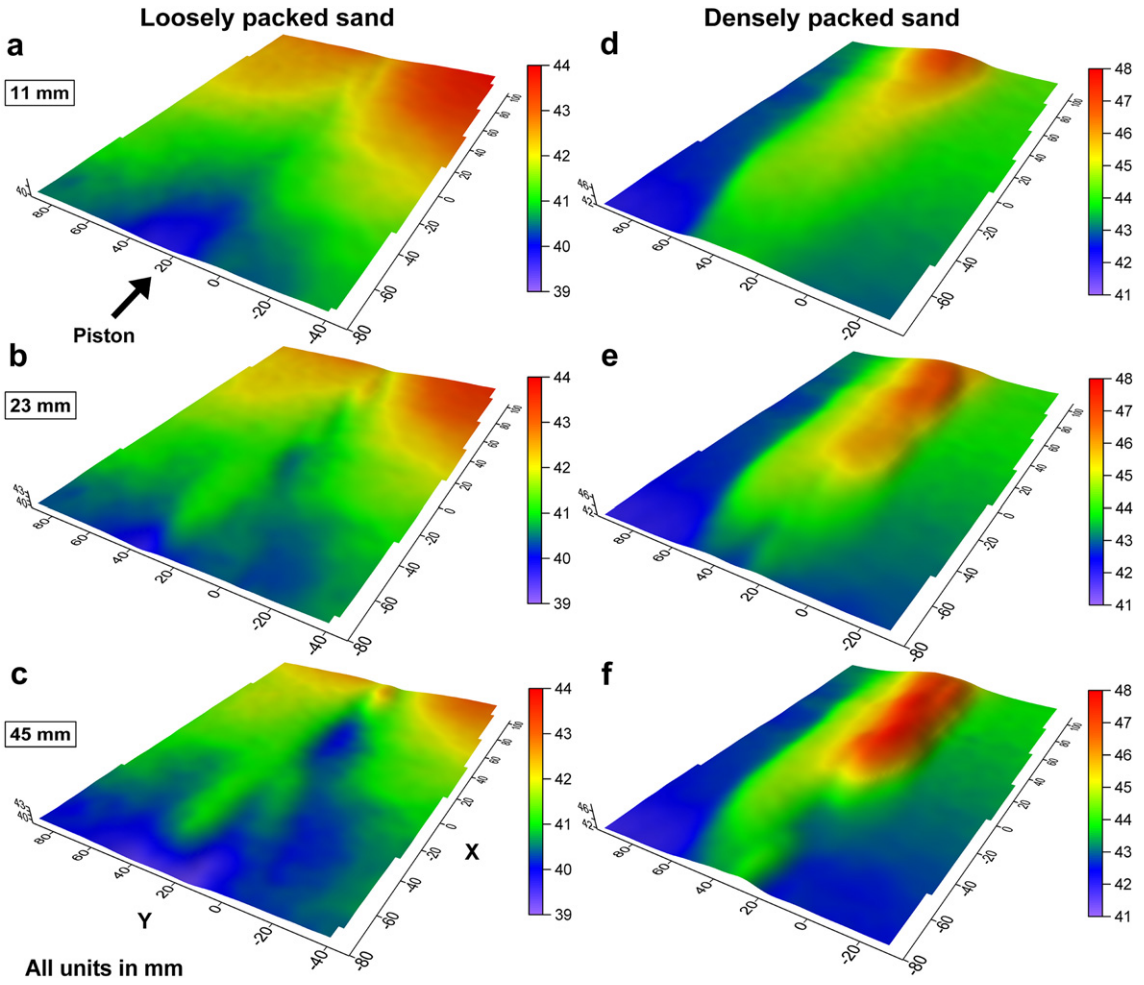

Fig. 2. Evolution of topography for both loose and dense sand. Colour scales denote model elevation in mm. Vertical exaggeration is 2:1. Finite displacement is given in boxes on the left. Whole-surface subsidence in loose sand propagates away from the piston because of vibrations transferred from the adjacent stepper motor. Shear-induced compaction clearly produces a graben-like basin (c.f., Fig. 3).

Only the model surface is monitored in 3D, but we can infer the cross-sectional geometry from previous work, surface observations, and the applied velocity boundary conditions. The faults branch off the basal velocity discontinuity resembling flower structures (Fig. 5a) with helicoidal Riedel shears (Le Guerroué and Cobbold, 2006; McClay and Dooley, 1995; Naylor et al., 1986; Richard et al., 1995; Ueta et al., 2000). The intersection of fault surface traces and model topography indicates that faults in the model centre are sub-vertical near the surface (Fig. 3). However, most faults are Riedel shears and therefore must change dip deeper in the sand layer because they emerge from the central velocity discontinuity. The PIV data illustrate that vertical shear deformation is localized along the Riedel shears (Fig. 4). Strike-slip faults in loose sand have a normal-slip component (Fig. 4a) with a mean incremental shear strain $Ezy = dD_z/dy$, of 0.5–1% at the surface. Those in dense sand have a reverse-slip component (Fig. 4b) with a surficial mean incremental *Ezy* between 1% and 2%.

4. Discussion: comparison to nature

Our results show that, at the laboratory scale, basement-driven simple shearing of loose sand produces negative topography with a narrow surface fault network while positive topography and a broader fault network develop in dense sand. This is in geometrical agreement with some natural examples (Fig. 5, Table 1). The physical explanation for this difference is straightforward. Loose sand responds to stress by compacting, leading to volume loss, subsidence and associated oblique-normal faulting. In contrast, dense sand dilates to accommodate deformation. The associated volume increase generates positive topography and faults with a reverse-slip component (Braun, 1994; Le Guerroué and Cobbold, 2006; Schöpfer and Steyrer, 2001). Shear-induced compaction compensates any dilatancy in loose sand as in some deformation experiments with porous rocks (Paterson and Wong, 2005). To which extent do fault network geometries and volume changes in our experiments scale up to nature? In the following, both model fault network geometrical parameters and volume changes are compared to natural data.

4.1. Scalability of fault zone geometry and fault width

We test the scalability of our models qualitatively by comparing their geometry to that of natural flower structures (Fig. 5a). Measurements of cross-sectional aspect ratios of natural fault zones ranging from 500 m to 36 km in width derived from seismic, structural, as well as earthquake-hypocenter cross-sections (Fig. 5, see Table 1 for references and data) show that the modelling results are upper-bound estimates of natural geometries.

The tendency to overestimate topography and fault zone width results from the simplicity of our setup. The 2–4 mm width of individual model faults is mainly controlled by the mean grain size

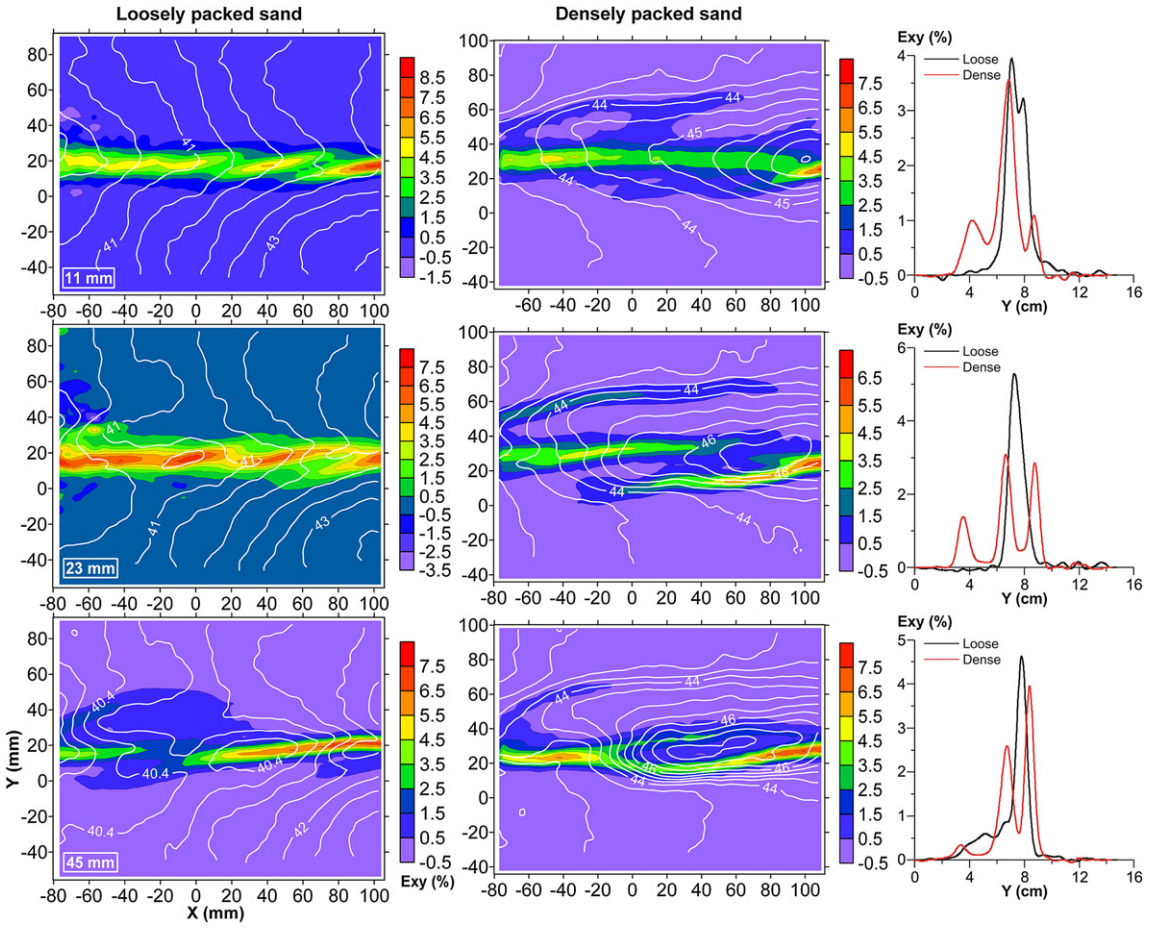

Fig. 3. Maps of incremental shear strain (*Exy* in %) for both sand types with associated vertical strain profiles through the map centre. Colour scales indicate horizontal shear strain in %. White contour lines denote model topography in mm. Finite displacement is given in boxes in lower left corner of the maps on the left.

(Desrues and Viggiani, 2004) of our sand. The faults appear wider in the strain maps (Fig. 3) because the displacement field resolution is 2×2 mm^2. Assuming a length scaling factor of 4×10^{-6} (4 cm in the model = 10 km in nature), individual model fault width scales to 500–1000 m. This is well within natural bounds (Watterson, 1986). Yet more localized, smaller faults cannot occur in sand in contrast to natural fault zones. In other words, natural size-frequency distributions of faults cannot be reproduced in physical models with granular materials. Therefore, fault volume and volume changes are probably overestimated.

4.2. Scalability of porosity and volume change

Dilatancy is common in brittle rocks (Jaeger and Cook, 1979; Paterson and Wong, 2005). Most quantitative measures stem from rock deformation experiments and are rarely constrained on natural length scales. A volume increase of ~6% is reported for Carrara marble in uniaxial experiments at 100 MPa confining pressure, decreasing to ~2.5% at 200 MPa (Edmond and Paterson, 1972). Sagan and Hart (2006) find a porosity increase from ~2% in limestone host rocks to 8% in a 100 m-scale positive flower structure in

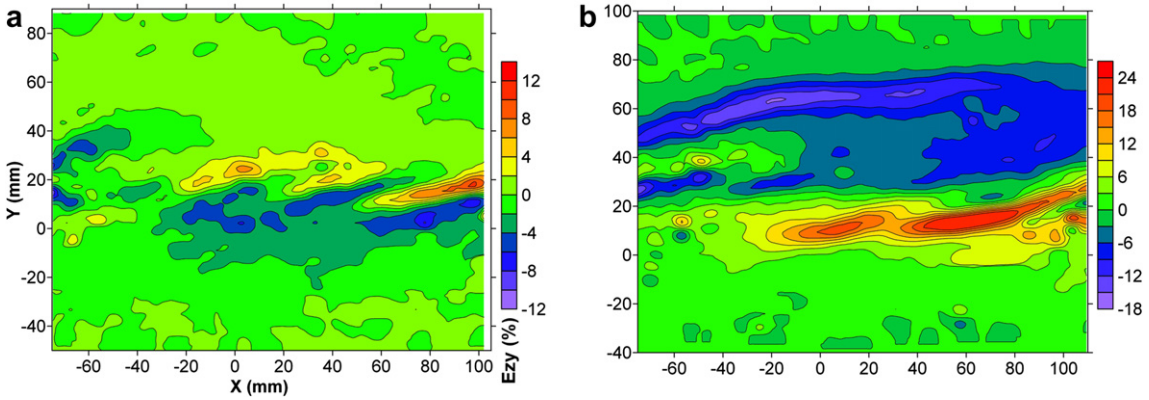

Fig. 4. Maps of cumulative vertical shear strain, *Ezy*, after 23 mm displacement in (a) loose and (b) dense sand. Colour scales indicate *Ezy* in %. Vertical shear strain is clearly localized along Riedel shears in both cases. Note the correlation with faults shown in central panel of Fig. 3.

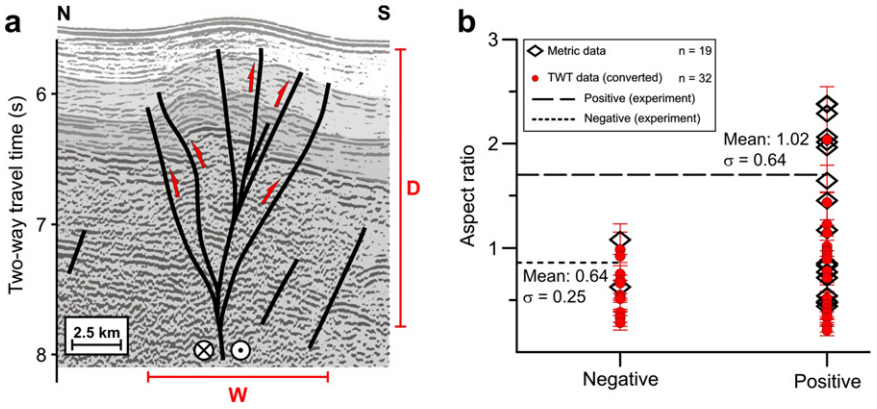

Fig. 5. a) Seismic profile of a positive flower structure from the Aruba Gap Abyssal Plain, Colombia (modified from Harding (1985)). Bars next to the image illustrate how width (W) and height (D) are measured for aspect ratio determination. b) Aspect ratios of negative and positive flower structures derived from seismic, structural, and earthquake-hypocenter cross-sections (see Table 1). Since most seismic images provide the vertical dimension in units of two-way travel time (data points with circular symbols), there is some uncertainty in the height measurements. We assume mean seismic velocities of 5 km/s (Wood and Treitel, 1975) for the height conversion and plot error bars for ± 1 km/s. Width measurements are corrected for orientation of cross-sections. Mean aspect ratios for model fault networks with positive and negative topography (dashed lines) are computed in the model centre after 5 cm displacement. Mean values and standard deviation for natural data are plotted.

the Trenton-Black River gas field. Onishi and Shimizu (2005) measure dilation in borehole samples of undeformed granite from 2% porosity to 8% in deformed granite in a km-scale fault. We find 5.1% bulk volume increase in the compacted sand model fault zone.

Shear-induced mechanical compaction is observed in deformation experiments on sandstone (Wong and Baud, 1999) and even occurs in compact limestone (Wong et al., 2003). A hydrostatic volume loss of 17% at 5 km depth is estimated for sandstone with an initial surface porosity of 31%, increasing to 24% at 10 km (Sheldon and Retallack, 2001). Shale and sandstone exhibit a hydrostatic porosity loss from 50% to about 5% from 100 m to 6 km depth (Baldwin and Butler, 1985). Theoretical models and field data suggest a possible volume loss of >50% for certain ductile shear zones (Baird and Hudleston, 2007; O'Hara, 1990). Compaction can cause displacement loss ≤20% in growth faults (Taylor et al., 2008). Ring et al. (2001) find a volume loss of 36% induced by solution-mass-transfer deformation in sandstone adjacent to the Glarus thrust. Shear-induced compaction in our models amounts to 4.2% volume decrease in the fault zone.

The experimental volume changes seem to be well within the natural parameter range and even underestimate those possible in porous sedimentary rocks. However, shear-induced dilatancy and compaction in nature might be more localized, i.e., focused in faults and their damage zones (Aydin, 2000; Micarelli et al., 2006; Shipton and Cowie, 2001) rather than distributed over an entire fault-bound wedge as in our experiments. If this were the case, our models would overestimate natural volume changes. We suspect that this may partly reflect measurement bias in natural settings. Due to common observational limitations caused by outcrop conditions, sparse samples, 2D sampling, etc., field-based porosity studies rarely provide a multi-scale 3D assessment of porosity distributions (Liu et al., 2009) in fault networks on ≥100-m scales. Moreover, uniform volumetric background strain affecting both host rocks and faults is difficult to recognize. Therefore, considerable volume changes on distributed small-scale structures and due to background strain might be overlooked in the field. Indeed, recent 3D seismic attribute-based porosity mapping of >100 m wide positive flower structures related to a 5.5 km long strike-slip fault reveals a porosity increase of ~6% for the material between the limbs of the flower structures (Sagan and Hart, 2006), suggesting that entire fault-bound wedges dilate. In addition, Ring et al. (2001) state that volume loss due to solution-mass-transfer is pervasive and diffuse in low-grade rocks and becomes increasingly localized into shear zones with increasing metamorphic grade. We therefore conclude that syndeformational volume changes in nature can affect large rock masses, especially in low-grade sedimentary rocks, and thus may have a major impact on fault network structure and topography along strike-slip faults.

We also note that model volume changes are integrated over the entire fault zone because surface elevation is the only proxy available. In fact, the model fault wedges do not experience uniform volume changes. 3D shear experiments monitored with CT scanners show that faults in sand also dilate and compact locally (Schreurs, 1994; Ueta et al., 2000), and the smallest faults in our experiments are below PIV resolution. Fig. 4 shows that vertical shear strains are localized along Riedel shears in our models implying domains of more localized volume change rather than homogeneous swelling/sinking of the entire model fault zone.

In nature, porosity decreases with depth. Additional spatial variability is introduced by varying material properties, e.g., lithology, fluid content, and grain size (Paterson and Wong 2005). Thus, the potential for volume change decreases with depth and effective pressure. Yet our models have uniform initial porosity. This contributes to an overestimation of topography. Moreover, volume changes in our models are solely caused by particulate flow and do not include other mechanisms occurring in nature (Edmond and Paterson, 1972; Wong et al., 2003). Therefore, biased stress scaling is expected.

Nevertheless, there is fundamental uncertainty regarding the magnitude and 3D distribution of syndeformational volume changes in natural rocks, in particular on large length scales. Despite their simplicity, our experiments emphasize the significant structural and topographic influence of deformation-induced volume changes in strike-slip settings. Comprehensive 3D multi-scale field studies of volume changes, porosity distribution, and the associated deformation are required to constrain better-scaled forward modelling experiments.

5. Summary and implications

We argue that the degree of host rock compaction likely will influence the development of topography and fault networks in strike-slip settings in sedimentary basins for the following reasons. 1) The potential for volume changes in the upper 5–10 km of sedimentary basins clearly exceeds the volume changes required to generate model topography. 2) Our models tend to overestimate topography and fault zone width and thus do not reproduce natural

Table 1
Data plotted in Fig. 5b and their references: 1) Hinsch et al. (2005); 2) Hsiao et al. (2004); 3) Itoh et al. (1998); 4) Mann (2007); 5) Sassi et al. (2006); 6) Bedir et al. (2001); 7) Doglioni (1987); 8) Fisher et al. (2003); 9) Fisher et al. (2004); 10) Hutchison (2005); 11) Jia et al. (2006); 12) Nicholas et al. (2007); 13) Picha (2002); 14) Ratchkovski et al. (2004); 15) Reston and Meissner (1989); 16) Ryan et al. (2008); 17) Sagan and Hart (2006); 18) Schattner et al. (2006); 19) Soeparyono and Lennox (1990); 20) Vidal et al. (2000).

Reference	Type	Width (m)	Metric height (m)	Height (twt/s)	Height (m) for 5 km/s
1, Fig. 5	–	6556		2.47	6165
1, Fig. 7	–	3399		1.83	4580
2, Fig. 14	–	4157		2.47	6163
2, Fig. 14	–	5527		2.9	7250
2, Fig. 14	–	1684		2.35	5875
2, Fig. 8	–	4012		2.63	6580
3, Fig. 7	–	716	1135		
3, Fig. 7	–	1724	1584		
4, Fig. 42	–	566		0.65	1633
4, Fig. 42	–	960		0.7	1745
4, Fig. 42	–	473		0.46	1138
5, Fig. 4	–	4500		2.35	5865
5, Fig. 4	–	5306		1.93	4823
6, Fig. 7	+	7241		3.12	7798
7, Fig. 8	+	1708	3878		
7, Fig. 8	+	2727	5454		
8, Fig. 14	+	528		0.56	1400
9, Fig. 14	+	12 099	8049		
9, Fig. 14	+	16 298	8049		
9, Fig. 14	+	19 753	8292		
2, Fig. 10	+	8160		1.6	4000
2, Fig. 5	+	2481		4.72	11 800
2, Fig. 8	+	7485		2.08	5193
10, Fig. 29	+	6021		2.1	5255
10, Fig. 29	+	7780		2.54	6340
11, Fig. 5	+	21 594	10 444		
4, Fig. 41	+	1884	2211		
4, Fig. 41	+	2326	3057		
4, Fig. 55	+	6480		3.66	9150
12, Fig. 11	+	1312		1.37	3420
12, Fig. 11	+	2249		0.99	2473
12, Fig. 11	+	937		1.43	3578
13, Fig. 4	+	16 642	14 205		
13, Fig. 4	+	13 529	15 887		
13, Fig. 5	+	6389		3.58	8945
13, Fig. 5	+	3002		2.88	7198
13, Fig. 5	+	5918		3.31	8275
14, Fig. 3_1	+	28 641	12 000		
14, Fig. 3_2	+	32 390	13 938		
14, Fig. 3_2	+	36 487	18 585		
15, Fig. 5	+	11 159		4.39	10 965
16, Fig. 7	+	1185	1334		
16, Fig. 7	+	759	1218		
17, Fig. 10	+	768	430		
18, Fig. 4	+	8103		2.79	6968
18, Fig. 4b_1	+	4791		3.32	8298
18, Fig. 4b_2	+	3591		1.75	4373
18, Fig. 4b_2	+	4647		2.57	6413
19, Fig. 6	+	6118		2.51	6270
19, Fig. 6	+	5010		2.57	6425
20, Fig. 5	+	3358	6366		

Profile angle	Corrected width (m)	Metric AR	AR for TWT data	AR error (±1 km/s)
68	6079		0.99	0.25
45	2403		0.52	0.13
80	4094		0.66	0.17
80	5443		0.75	0.19
80	1658		0.28	0.07
64	3606		0.55	0.14
83	711	0.63		
83	1711	1.08		
72	538		0.33	0.08
69	896		0.51	0.13
67	435		0.38	0.1
64	4045		0.69	0.17
57	4450		0.92	0.23
85	7213		0.93	0.23
90	1708	0.44		
76	2646	0.49		
86	527		0.38	0.09
75	11 687	1.45		

(*continued on next page*)

Table 1 (*continued*)

Profile angle	Corrected width (m)	Metric AR	AR for TWT data	AR error (±1 km/s)
84	16 209	2.01		
90	19 753	2.38		
87	8149		2.04	0.51
90	2481		0.21	0.05
84	7444		1.43	0.36
90	6021		1.15	0.29
90	7780		1.23	0.31
86	21 541	2.06		
90	1884	0.85		
70	2186	0.71		
90	6480		0.71	0.18
79	1288		0.38	0.09
79	2208		0.89	0.22
79	920		0.26	0.06
89	16 639	1.17		
78	13 233	0.83		
87	6380		0.71	0.18
87	2998		0.42	0.1
87	5910		0.71	0.18
85	28 532	2.38		
80	31 898	2.29		
89	36 481	1.96		
88	11 152		1.02	0.25
60	1026	0.77		
60	657	0.54		
67	707	1.64		
56	6718		0.96	0.24
35	2748		0.33	0.08
39	2260		0.52	0.13
39	2924		0.46	0.11
88	6114		0.98	0.24
88	5007		0.78	0.19
64	3018	0.47		

volume changes accurately. However, we demonstrate that our models satisfy geometrical similarity with natural fault zones, and that the aspect ratios of model flower-structure coincide with upper-bound estimates of natural examples considered here (mean + 1σ, Fig. 5). The widths of individual model faults also scale up reasonably, even for small scaling factors. 3) Volume changes and 3D porosity distributions in large-scale natural fault networks are poorly constrained. Available 3D porosity distributions of natural flower structures (Sagan and Hart, 2006) are similar to those observed in our models and imply that shear-induced volume changes may be more distributed than previously suggested. We therefore suspect that syndeformational volume changes in natural fault networks can add up to about 5% as seen in our experiments. Thus, compaction and dilatancy should be considered in mechanical forward models of strike-slip faults. For example, 3D physical experiments observed with CT scanners could probe the effect of depth-dependent porosity, map volume changes more precisely and estimate cut-off depths for compaction-controlled volume changes. Numerical modelling could evaluate the impact of other volume change mechanisms such as grain crushing or pressure solution which is important at depths greater than 4.5 km (Ring et al., 2001; Wong et al., 2003). In addition, topography can affect fault orientation (Fialko et al., 2005), fault-slip direction (Cowgill et al., 2004), fault strength (Koons et al., 2002), and fluid flow through faults and their host rocks (Fulton et al., 2004; Lopez and Smith, 1995). Therefore, our results suggest that syndeformational volume changes might have a considerable impact on the complex interplay of material properties, stress- and kinematic-boundary conditions, topography, fluid flow, and geometry in strike-slip fault networks.

Acknowledgements

P. Cobbold, K.J.W. McCaffrey, A. Meigs, P.-Y. Robin, and J. Waldron are thanked for constructive comments on a previous version of this paper. We gratefully acknowledge helpful reviews from referee S. Johnson and Editor J. Hippertt. Funding was provided by the University of Toronto and a Natural Sciences and Engineering Council of Canada Discovery Grant to ARC.

References

Adam, J., Urai, J.L., Wieneke, B., Oncken, O., Pfeiffer, K., Kukowski, N., Lohrmann, J., Hoth, S., van der Zee, W., Schmatz, J., 2005. Shear localisation and strain distribution during tectonic faulting–new insights from granular-flow experiments and high-resolution optical image correlation techniques. Journal of Structural Geology 27 (2), 283–301.

Aydin, A., 2000. Fractures, faults, and hydrocarbon entrapment, migration and flow. Marine and Petroleum Geology 17 (7), 797–814.

Baird, G.B., Hudleston, P.J., 2007. Modeling the influence of tectonic extrusion and volume loss on the geometry, displacement, vorticity, and strain compatibility of ductile shear zones. Journal of Structural Geology 29 (10), 1665–1678.

Baldwin, B., Butler, C.O., 1985. Compaction curves. American Association of Petroleum Geologists Bulletin 69 (4), 622–626.

Bedir, M., Boukadi, N., Tlig, S., Ben Timzal, F., Zitouni, L., Alouani, R., Slimane, F., Bobier, C., Zargouni, F., 2001. Subsurface mesozoic basins in the central atlas of Tunisia: tectonics, sequence deposit distribution, and hydrocarbon potential. American Association of Petroleum Geologists Bulletin 85 (5), 885–907.

Bergerat, F., Angelier, J., Gudmundsson, A., Torfason, H., 2003. Push-ups, fracture patterns, and palaeoseismology of the Leirubakki fault, South Iceland. Journal of Structural Geology 25 (4), 591–609.

Braun, J., 1994. Three-dimensional numerical simulations of crustal-scale wrenching using a non-linear failure criterion. Journal of Structural Geology 16 (8), 1173–1186.

Cowgill, E., Yin, A., Arrowsmith, J.R.n., Feng, W.X., Shuanhong, Z., 2004. The Akato Tagh bend along the Altyn Tagh fault, northwest Tibet 1: smoothing by vertical-axis rotation and the effect of topographic stresses on bend-flanking faults. Geological Society of America Bulletin 116 (11–12), 1423–1442.

Desrues, J., Viggiani, G., 2004. Strain localization in sand: an overview of the experimental results obtained in Grenoble using stereophotogrammetry. International Journal for Numerical and Analytical Methods in Geomechanics 28 (4), 279–321.

Doglioni, C., 1987. Tectonics of the dolomites (southern Alps, northern Italy). Journal of Structural Geology 9 (2), 181–193.

Dresen, G., 1991. Stress distribution and the orientation of riedel shears. Tectonophysics 188 (3–4), 239–247.

Edmond, J.M., Paterson, M.S., 1972. Volume changes during the deformation of rocks at high pressures. International Journal of Rock Mechanics and Mining Sciences 9 (2), 161–182.

Fialko, Y., Rivera, L., Kanamori, H., 2005. Estimate of differential stress in the upper crust from variations in topography and strike along the San Andreas fault. Geophysical Journal International 160 (2), 527–532.
Fisher, M.A., Normark, W.R., Bohannon, R.G., Sliter, R.W., Calvert, A.J., 2003. Geology of the continental margin beneath Santa Monica Bay, southern California, from seismic-reflection data. Bulletin of the Seismological Society of America 93 (5), 1955–1983.
Fisher, M.A., Ratchkovski, N.A., Nokleberg, W.J., Pellerin, L., Glen, J.M.G., 2004. Geophysical data reveal the crustal structure of the Alaska range Orogen within the Aftershock zone of the Mw 7.9 Denali fault earthquake. Bulletin of the Seismological Society of America 94 (6B), S107–S131.
Fulton, P.M., Saffer, D.M., Harris, R.N., Bekins, B.A., 2004. Re-evaluation of heat flow data near Parkfield, CA: evidence for a weak San Andreas fault. Geophysical Research Letters 31 (15), 1–4. L15S15.
Harding, T.P., 1985. Seismic characteristics and identification of negative flower structures, positive flower structures, and positive structural inversion. American Association of Petroleum Geologists Bulletin 69 (4), 582–600.
Hinsch, R., Decker, K., Wagreich, M., 2005. 3-D mapping of segmented active faults in the southern Vienna Basin. Quaternary Science Reviews 24 (3–4), 321–336.
Hsiao, L.-Y., Graham, S.A., Tilander, N., 2004. Seismic reflection imaging of a major strike-slip fault zone in a rift system: Paleogene structure and evolution of the Tan-Lu fault system, Liaodong Bay, Bohai, offshore China. American Association of Petroleum Geologists Bulletin 88 (1), 71–97.
Hutchison, C.S., 2005. Miri zone. In: Geology of North-West Borneo. Elsevier, Amsterdam, pp. 77–134.
Itoh, Y., Takemura, K., Kamata, H., 1998. History of basin formation and tectonic evolution at the termination of a large transcurrent fault system: deformation mode of central Kyushu, Japan. Tectonophysics 284 (1–2), 135–150.
Jaeger, J.C., Cook, N.G.W., 1979. Fundamentals of Rock Mechanics. Chapman and Hall, United Kingdom (GBR), London.
Jia, D., Wei, G., Chen, Z., Li, B., Zeng, Q., Yang, G., 2006. Longmen Shan fold-thrust belt and its relation to the western Sichuan Basin in central China: new insights from hydrocarbon exploration. American Association of Petroleum Geologists Bulletin 90 (9), 1425–1447.
Koons, P.O., Henderson, C.M., 1995. Geodetic analysis of model oblique collision and comparison to the Southern Alps of New Zealand. New Zealand Journal of Geology and Geophysics 38 (4), 545–552.
Koons, P.O., Zeitler, P.K., Chamberlain, C.P., Craw, D., Meltzer, A.S., 2002. Mechanical links between erosion and metamorphism in Nanga Parbat, Pakistan Himalaya. American Journal of Science 302 (9), 749–773.
Krantz, R.W., 1991. Measurements of friction coefficients and cohesion for faulting and fault reactivation in laboratory models using sand and sand mixtures. Tectonophysics 188 (1–2), 203–207.
Le Guerroué, E., Cobbold, P.R., 2006. Influence of erosion and sedimentation on strike-slip fault systems: insights from analogue models. Journal of Structural Geology 28 (3), 421–430.
Liu, J., Regenauer-Lieb, K., Hines, C., Liu, K., Gaede, O., Squelch, A., 2009. Improved estimates of percolation and anisotropic permeability from 3-D X-ray microtomography using stochastic analyses and visualization. Geochemistry, Geophysics, Geosystems 10.
Lohrmann, J., Kukowski, N., Adam, J., Oncken, O., 2003. The impact of analogue material properties on the geometry, kinematics, and dynamics of convergent sand wedges. Journal of Structural Geology 25 (10), 1691–1711.
Lopez, D.L., Smith, L., 1995. Fluid flow in fault zones: analysis of the interplay of convective circulation and topographically driven groundwater flow. Water Resources Research 31 (6), 1489–1503.
Mann, P., 2007. Global catalogue, classification and tectonic origins of restraining- and releasing bends on active and ancient strike-slip fault systems. Geological Society, London, Special Publications 290 (1), 13–142.
McClay, K., Dooley, T., 1995. Analogue models of pull-apart basins. Geology 23 (8), 711–714.
Micarelli, L., Benedicto, A., Wibberley, C.A.J., 2006. Structural evolution and permeability of normal fault zones in highly porous carbonate rocks. Journal of Structural Geology 28 (7), 1214–1227.
Mourgues, R., Cobbold, P., 2003. Some tectonic consequences of fluid overpressures and seepage forces as demonstrated by sandbox modelling. Tectonophysics 376 (1–2), 75–97.
Naylor, M.A., Mandl, G., Supesteijn, C.H.K., 1986. Fault geometries in basement-induced wrench faulting under different initial stress states. Journal of Structural Geology 8 (7), 737–752.
Nicholas, C.J., Pearson, P.N., McMillan, I.K., Ditchfield, P.W., Singano, J.M., 2007. Structural evolution of southern coastal Tanzania since the Jurassic. Journal of African Earth Sciences 48 (4), 273–297.
O'Hara, K., 1990. State of strain in mylonites from the western Blue Ridge province, southern Appalachians: the role of volume loss. Journal of Structural Geology 12 (4), 419–430.
Onishi, C.T., Shimizu, I., 2005. Microcrack networks in granite affected by a fault zone: visualization by confocal laser scanning microscopy. Journal of Structural Geology 27 (12), 2268–2280.
Paterson, M.S., Wong, T.-f, 2005. Experimental Rock Deformation; the Brittle Field. Springer-Verlag, Berlin, Federal Republic of Germany (DEU), Berlin.
Picha, F.J., 2002. Late orogenic strike-slip faulting and escape tectonics in frontal Dinarides–Hellenides, Croatia, Yugoslavia, Albania, and Greece. American Association of Petroleum Geologists Bulletin 86 (9), 1659–1671.
Ratchkovski, N.A., Wiemer, S., Hansen, R.A., 2004. Seismotectonics of the central Denali fault, Alaska, and the 2002 Denali fault earthquake sequence. Bulletin of the Seismological Society of America 94 (6B), S156–S174.
Reston, T., Meissner, R., 1989. The three-dimensional structure of the Oberpfalz – an alternative interpretation of the dEKORP-KTB data. Tectonophysics 157 (1–3), 1–11.
Richard, P.D., Naylor, M.A., Koopman, A., 1995. Experimental models of strike-slip tectonics. Petroleum Geoscience 1 (1), 71–80.
Ring, U., Brandon, M.T., Ramthun, A., 2001. Solution-mass-transfer deformation adjacent to the Glarus Thrust, with implications for the tectonic evolution of the Alpine wedge in eastern Switzerland. Journal of Structural Geology 23 (10), 1491–1505.
Ryan, H.F., Parsons, T., Sliter, R.W., 2008. Vertical tectonic deformation associated with the San Andreas fault zone offshore of San Francisco, California. Tectonophysics 457 (3–4), 209–223.
Sagan, J.A., Hart, B.S., 2006. Three-dimensional seismic-based definition of fault-related porosity development: Trenton-Black river interval, Saybrook, Ohio. American Association of Petroleum Geologists Bulletin 90 (11), 1763–1785.
Sassi, M.H., Zouari, H., Jallouli, C., 2006. Contribution de la gravimétrie et de la sismique réflexion pour une nouvelle interprétation géodynamique des fossés d'effondrement en Tunisie: exemple du fossé de Grombalia. Comptes Rendus Geosciences 338 (11), 751–756.
Schattner, U., Ben-Avraham, Z., Lazar, M., Hüebscher, C., 2006. Tectonic isolation of the Levant basin offshore Galilee–Lebanon – effects of the dead sea fault plate boundary on the Levant continental margin, eastern Mediterranean. Journal of Structural Geology 28 (11), 2049–2066.
Schöpfer, M.P.J., Steyrer, H.P., 2001. Experimental modeling of strike-slip faults and the self-similar behavior. In: Koyi, H., Mancktelow, N.S. (Eds.), Tectonic Modeling: A Volume in Honor of Hans Ramberg. Geological Society of America Memoir, vol. 193. Geological Society of America, Boulder.
Schreurs, G., 1994. Experiments on strike-slip faulting and block rotation. Geology 22 (6), 567–570.
Sheldon, N.D., Retallack, G.J., 2001. Equation for compaction of paleosols due to burial. Geology 29 (3), 247–250.
Shipton, Z.K., Cowie, P.A., 2001. Damage zone and slip-surface evolution over [mu]m to km scales in high-porosity Navajo sandstone, Utah. Journal of Structural Geology 23 (12), 1825–1844.
Soeparyono, N., Lennox, P.G., 1990. Structural development of hydrocarbon traps in the Cepu oil fields, northeast Java, Indonesia. Journal of Southeast Asian Earth Sciences 4 (4), 281–291.
Sylvester, A.G., 1988. Strike-slip faults. Geological Society of America Bulletin 100 (11), 1666–1703.
Taylor, S.K., Nicol, A., Walsh, J.J., 2008. Displacement loss on growth faults due to sediment compaction. Journal of Structural Geology 30 (3), 394–405.
Tchalenko, J.S., 1970. Similarities between shear zones of different Magnitudes. Geological Society of America Bulletin 81 (6), 1625–1640.
Ueta, K., Tani, K., Kato, T., 2000. Computerized X-ray tomography analysis of three-dimensional fault geometries in basement-induced wrench faulting. Engineering Geology 56 (1–2), 197–210.
Vidal, N., Alvarez-Marrón, J., Klaeschen, D., 2000. Internal configuration of the Levantine Basin from seismic reflection data (eastern Mediterranean). Earth and Planetary Science Letters 180 (1–2), 77–89.
Watterson, J., 1986. Fault dimensions, displacements and growth. Pure and Applied Geophysics 124 (1–2), 365–373.
Wong, T.-f., Baud, P., 1999. Mechanical compaction of porous sandstone. Oil and Gas Science and Technology 54 (6), 715–727.
Wong, T.-f., David, C., Menéndez, B., 2003. Chapter 2 mechanical compaction. In: Guéguen, Y., Boutéca, M. (Eds.), International Geophysics, vol. 89. Academic Press, pp. 55–114.